

Electronic Supplementary Information

Synergistic bimetallic CuPd oxide alloy

electrocatalyst for ammonia production from the

electrochemical nitrate reduction

*Wonsang Jun^{a,b,†}, Jaewoo Jeong^{c,‡}, Younghyun Chae^{a,b}, Woong Hee Lee^a, Young-Jin Ko^a,
Keun Hwa Chae^d, Hyung-suk Oh^{a,e}, Ung Lee^{a,b,f}, Dong Ki Lee^{a,b,f,k}, Byoung Koun Min^{a,f,g},
Hyeyoung Shin^{h*}, Yun Jeong Hwang^{i,j*}, and Da Hye Won^{a,b*}*

^aClean Energy Research Center, Korea Institute of Science and Technology (KIST), Seoul 02792, Republic of Korea

^bDivision of Energy and Environmental Technology, KIST School, Korea University of Science and Technology (UST), Seoul 02792, Republic of Korea

^cDepartment of Chemistry, Korea Advanced Institute of Science and Technology (KAIST), Daejeon 34141, Republic of Korea

^dAdvanced Analysis Center, Korea Institute of Science and Technology, Seoul 02792, Republic of Korea

^eKIST-SKKU Carbon-Neutral Research Center, Sungkyunkwan University 2066 Seobu-ro, Jangan-gu, Suwon 16419, Republic of Korea

^fGraduate School of Energy and Environment (Green School), Korea University, Seoul 02841, Republic of Korea.

^gClean Energy Institute, Korea Institute of Science and Technology (KIST), Seoul 02792, Republic of Korea

^hGraduate School of Energy Science and Technology (GEST), Chungnam National University, Daejeon 34134, Republic of Korea.

ⁱDepartment of Chemistry, Seoul National University, Seoul 08826, Republic of Korea.

^jCenter for Nanoparticle Research, Institute for Basic Science (IBS), Seoul 08826, Republic of Korea.

^kDepartment of Chemical and Biomolecular Engineering, Yonsei-KIST Convergence Research Institute, Yonsei University, Seoul 03722, Republic of Korea.

Corresponding Authors

Hyeyoung Shin – E-mail: shinhy@cnu.ac.kr,

Yun Jeong Hwang – E-mail: yjhwang1@snu.ac.kr,

Da Hye Won – E-mail: dahye0803@kist.re.kr

‡These authors contributed equally to this work.

Table of contents

Supplementary Notes

Supplementary Figure S1 ~ S16

Supplementary Table S1

Supplementary References

Supplementary Notes

Computational details

Spin-polarized density functional theory (DFT) calculations were carried out using the projector augmented-wave (PAW) method¹ and the Perdew-Burke-Ernzerhoff (PBE) functional,² as implemented in the Vienna Ab initio Simulation Package (VASP 5.4).³ The Grimme's DFT-D3 method⁴ was added to describe the van der Waals interactions. For the bulk models, a (6×6×6) Monkhorst–Pack k -point mesh⁵ and a plane-wave cutoff energy of 600 eV were used. The DFT-optimized lattice constants of bulk Cu and Pd are found to be 3.63 Å and 3.96 Å, respectively, which are in good agreement with the experimental values. (3.61 Å for Cu⁶ and 3.89 Å for Pd⁷) The most stable configuration of bulk Cu_{0.65}Pd_{0.35} with the lowest free energy was used among the fifteen randomly generated bulk Cu_{0.65}Pd_{0.35} alloy models (Figure S15) and the optimized lattice constant of the bulk Cu_{0.65}Pd_{0.35} is 3.77 Å, which is similar to the lattice constant of 3.71 Å estimated by the Vegard's law⁸. Based on the optimized bulk structures, the Cu (111), Cu_{0.65}Pd_{0.35} (111) and Pd (111) surfaces were modeled with four layers of a 4 × 4 supercell and a vacuum slab of 15 Å along the z direction. The Cu slab model and Pd slab model consist of 64 Cu atoms and 64 Pd atoms, respectively while the Cu_{0.65}Pd_{0.35} slab consists of 42 Cu atoms and 22 Pd atoms as shown in Figure S16. For the slab models, dipole correction was applied along the z direction and a (3×3×1) Monkhorst–Pack k -point mesh and a plane-wave cutoff energy of 400 eV were used. In addition, all slab models were optimized by fixing the bottom two layers and allowing the top two layers and adsorbates to relax. To calculate the free energy of each reaction step at room temperature (298.15 K), the zero-point energies, enthalpy, and entropy were calculated and the solvation effect was considered using the implicit solvation model implemented in VASPsol.^{9, 10}

All possible adsorption sites on the surface models were investigated and only the most stable adsorption configuration for each intermediate was considered for discussion in this work.

Specific capacitance calculation

Cyclic voltammetry (CV) was performed with Ar-purged 0.05 M Na₂SO₄ solution to obtain CV profiles of CuO_x, Cu_{0.94}Pd_{0.06}O_x, Cu_{0.89}Pd_{0.11}O_x, Cu_{0.65}Pd_{0.35}O_x, Cu_{0.33}Pd_{0.67}O_x, and Pd, respectively. CV was conducted with 10, 20, 30, 40, and 50 mV s⁻¹ scan rate, respectively. Specific capacitance was obtained from the slope of scan rate and current density.

Long-term eNO₃RR stability for Cu_{0.65}Pd_{0.35}O_x

3 cycle eNO₃RR was performed with chronoamperometric method in Ar-purged 0.1 M KNO₃ and -1.6 V (vs. Ag/AgCl) potential was applied during 104 h eNO₃RR. At first cycle, catholyte was sampled at 1.5, 15, 22.2 and 40 h, respectively. After the first cycle catholyte was changed to fresh Ar-purged 0.1 M KNO₃ and during second cycle catholyte was sampled 51, 61, 71, 81, 91, and 101 h, respectively. Similarly, after the second cycle catholyte was changed to fresh Ar-purged 0.1 M KNO₃ and during third cycle catholyte was sampled at 102 and 104 h, respectively. NH₃ conversion was derived from the following calculation where ΔC_{NH₃} and C_{NO₃} is the increase of accumulated NH₃ concentration and the initial nitrate concentration, respectively.

$$\text{NH}_3 \text{ conversion (\%)} = \Delta C_{\text{NH}_3} / C_{\text{NO}_3} \times 100 (\%)$$

Supplementary Figures

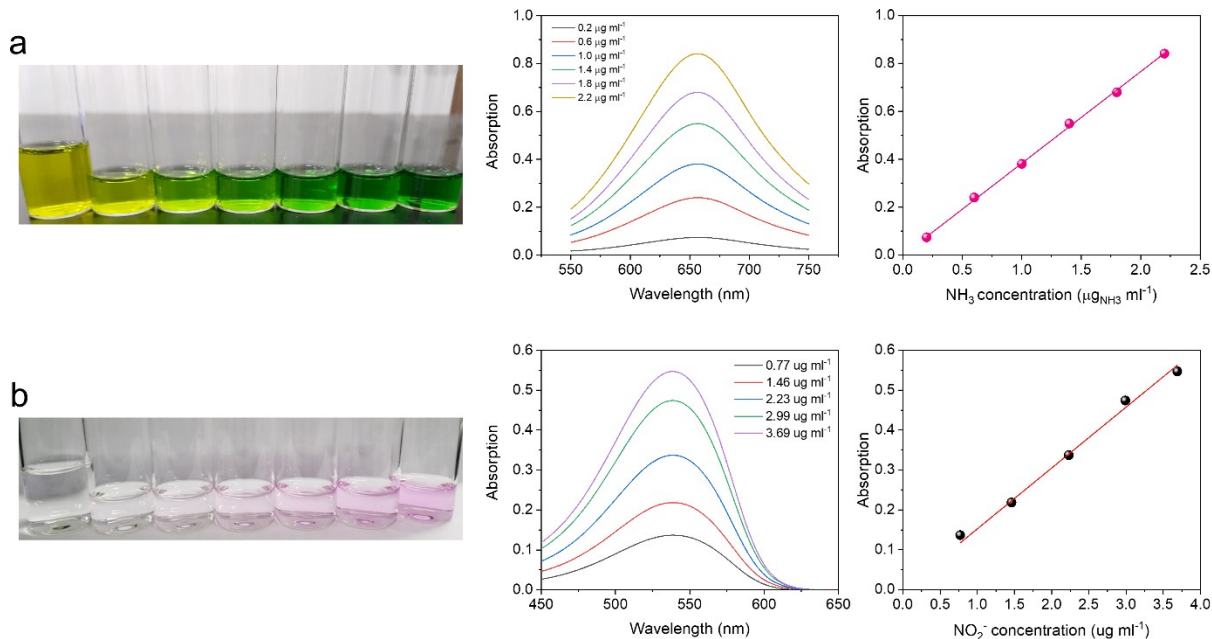


Fig. S1 e NO_3RR products quantification using UV-Vis spectroscopy colorimetric method. Digital images of catholyte after the reaction, absorption profiles as a function of wavelength and calibration curve of (a) indophenol method for NH_3 and (b) NO_2^- titration using Griess' reagent.

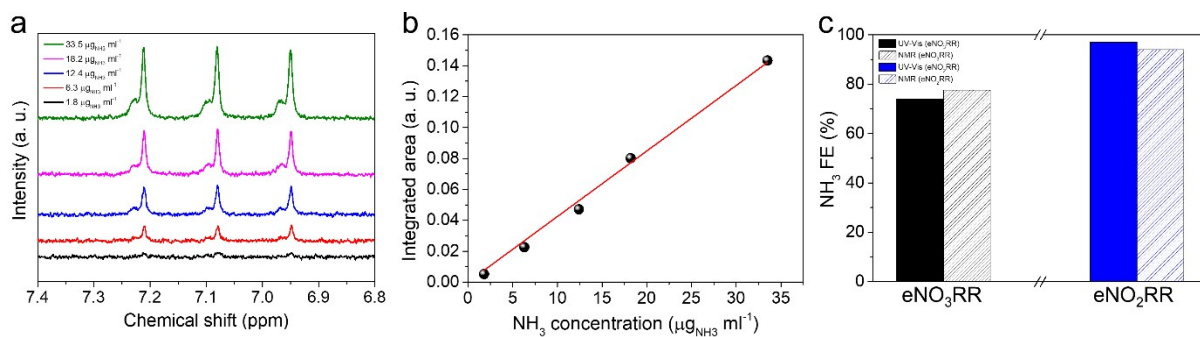


Fig. S2 e NO_3RR products quantification using NMR analysis. (a) NMR profiles for various NH_3 concentration. (b) Calibration curve. (c) FE comparison obtained from NMR and UV-Vis.

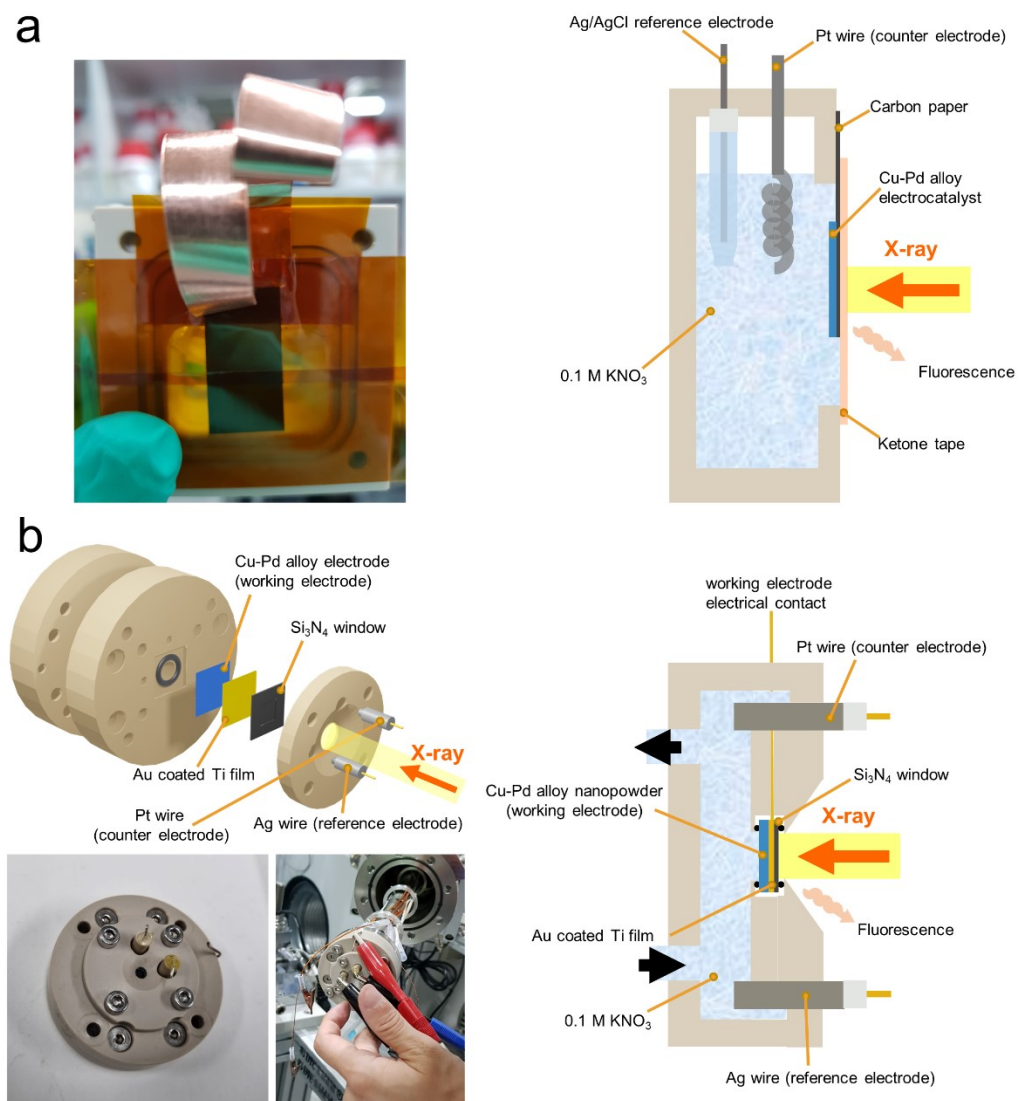


Fig. S3 *Operando* cell configuration. Digital and schematic images of an electrolysis cell for *operando* (a) XAFS and (b) NEXAFS.

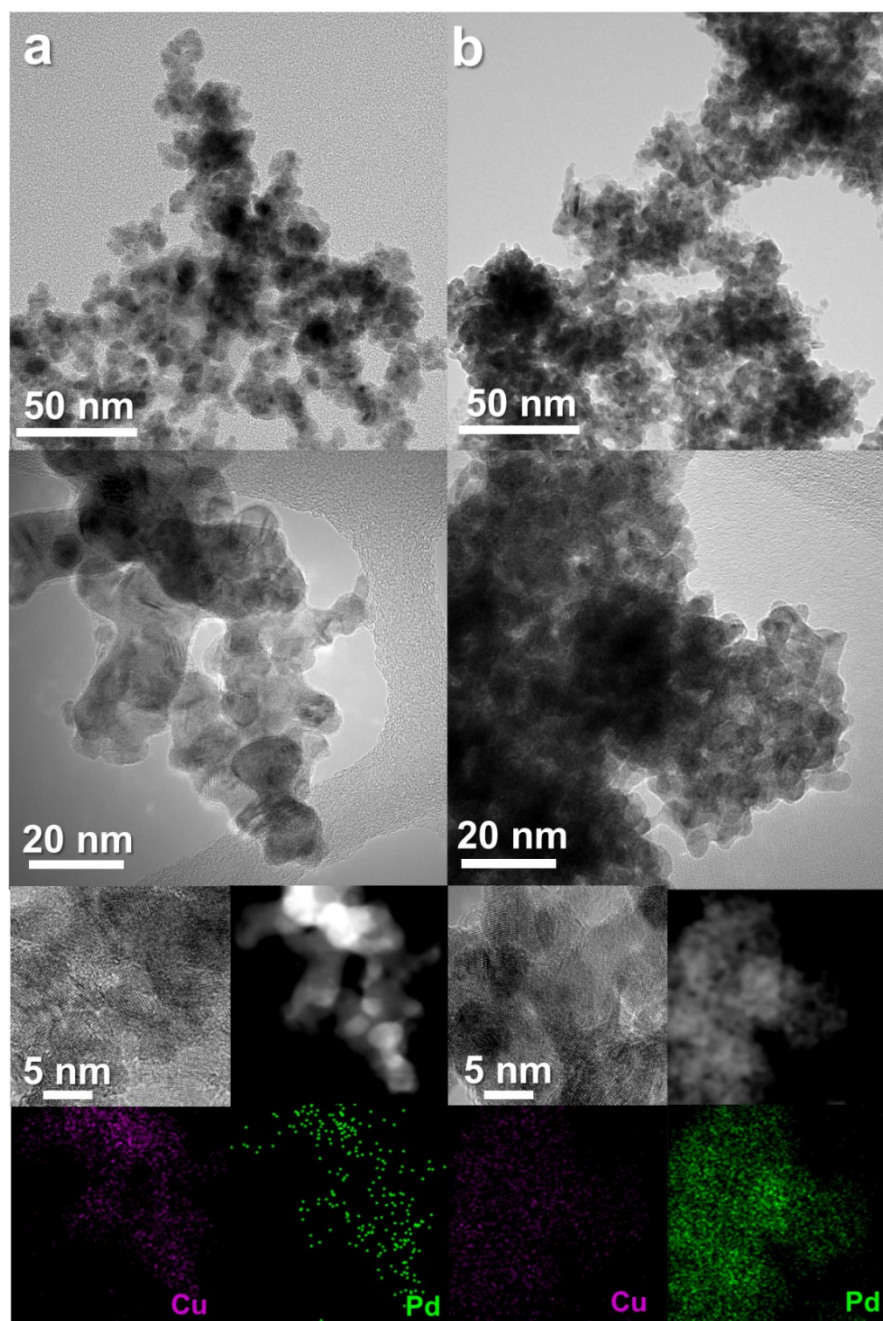


Fig. S4 Bright field TEM and EDS images of (a) $\text{Cu}_{0.89}\text{Pd}_{0.11}\text{O}_x$, (b) $\text{Cu}_{0.33}\text{Pd}_{0.67}\text{O}_x$.

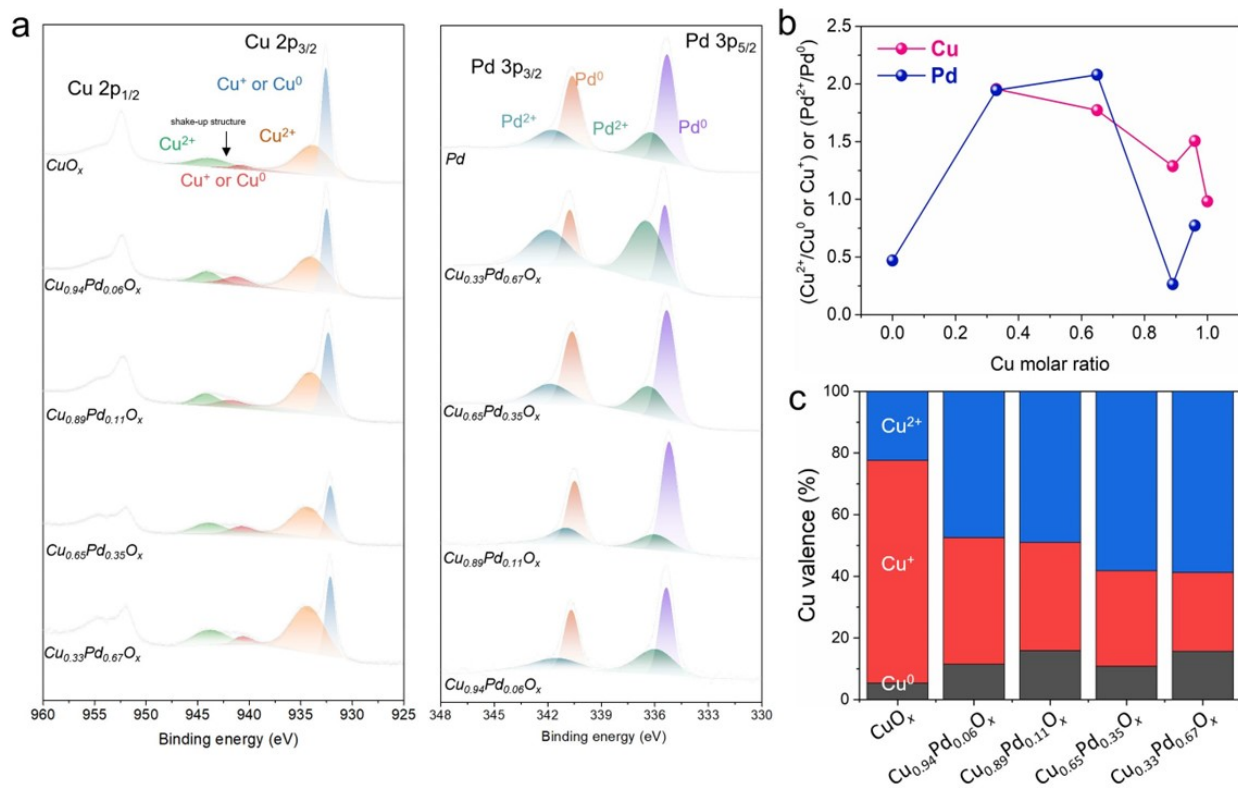


Fig. S5 Characterizations of the prepared catalysts. Profiles of (a) Cu 2p XPS and Pd 3p XPS. (b) Peak area ratios ($\text{Cu}^{2+}/\text{Cu}^0$ or Cu^+) and ($\text{Pd}^{2+}/\text{Pd}^0$) as a function of Cu molar ratio. (c) Proportion of Cu valence states calculated by linear combination of Cu K-edge XAFS.

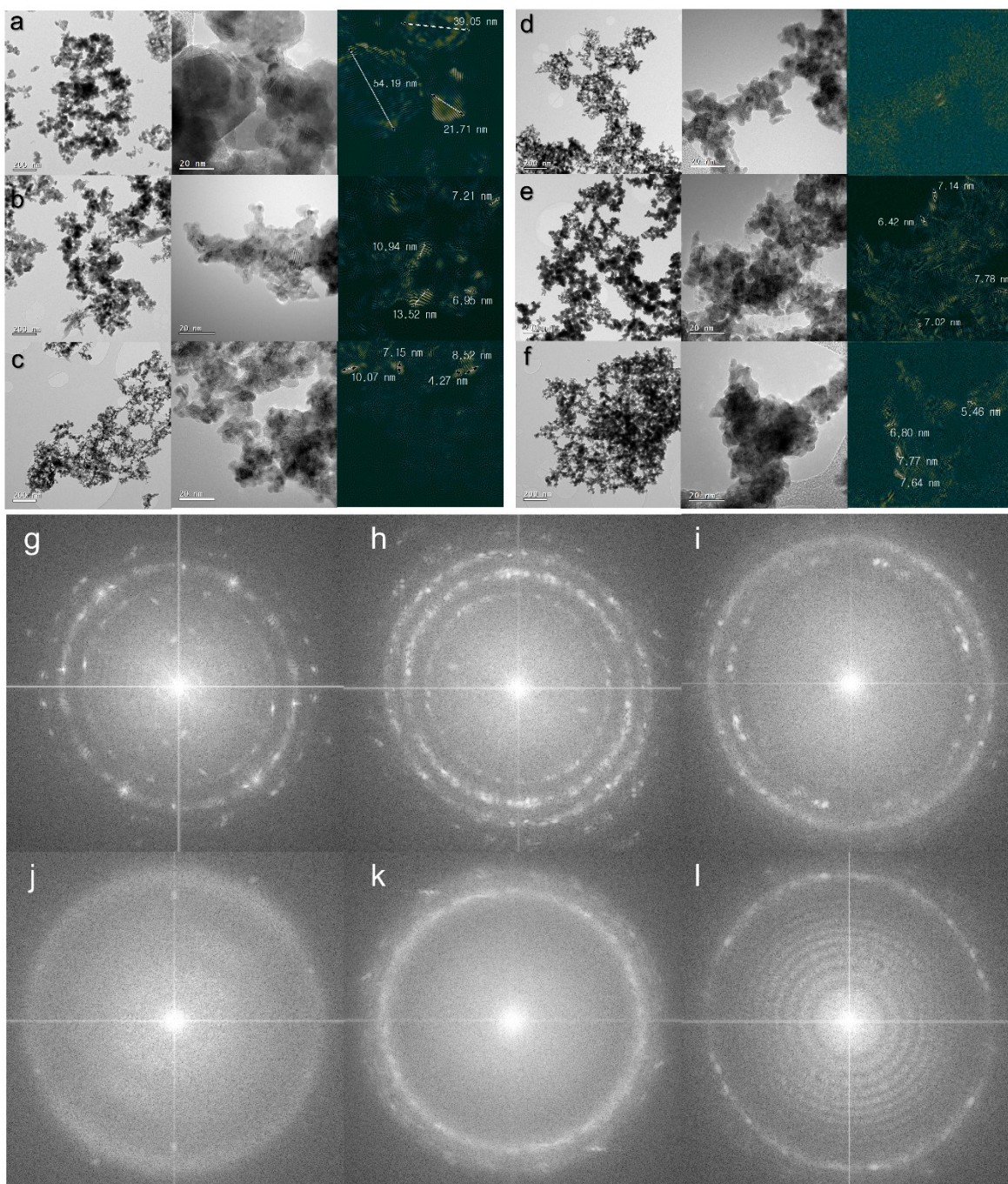


Fig. S6 TEM analysis. Bright field TEM and fast Fourier transformation image of (a) CuO_x , (b) $\text{Cu}_{0.94}\text{Pd}_{0.06}\text{O}_x$, (c) $\text{Cu}_{0.89}\text{Pd}_{0.11}\text{O}_x$, (d) $\text{Cu}_{0.65}\text{Pd}_{0.35}\text{O}_x$, (e) $\text{Cu}_{0.33}\text{Pd}_{0.67}\text{O}_x$, and (f) Pd. Inverse fast Fourier transformation image of (g) CuO_x , (h) $\text{Cu}_{0.94}\text{Pd}_{0.06}\text{O}_x$, (i) $\text{Cu}_{0.89}\text{Pd}_{0.11}\text{O}_x$, (j) $\text{Cu}_{0.65}\text{Pd}_{0.35}\text{O}_x$, (k) $\text{Cu}_{0.33}\text{Pd}_{0.67}\text{O}_x$, and (l) Pd.

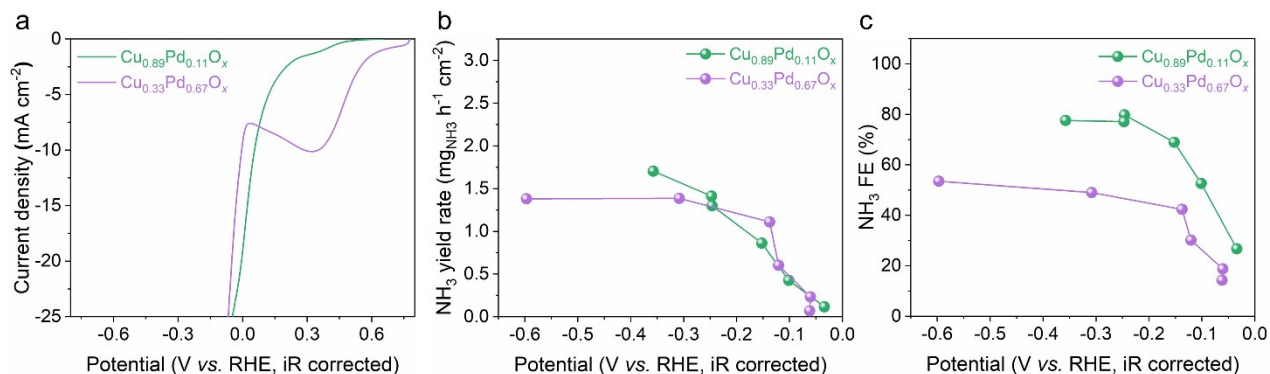


Fig. S7 e NO_3 RR performance of $\text{Cu}_{0.89}\text{Pd}_{0.11}\text{O}_x$ and $\text{Cu}_{0.33}\text{Pd}_{0.67}\text{O}_x$. (a) LSV with scan rate 5 mV s^{-1} , (b) NH_3 yield rate and (c) NH_3 FE.

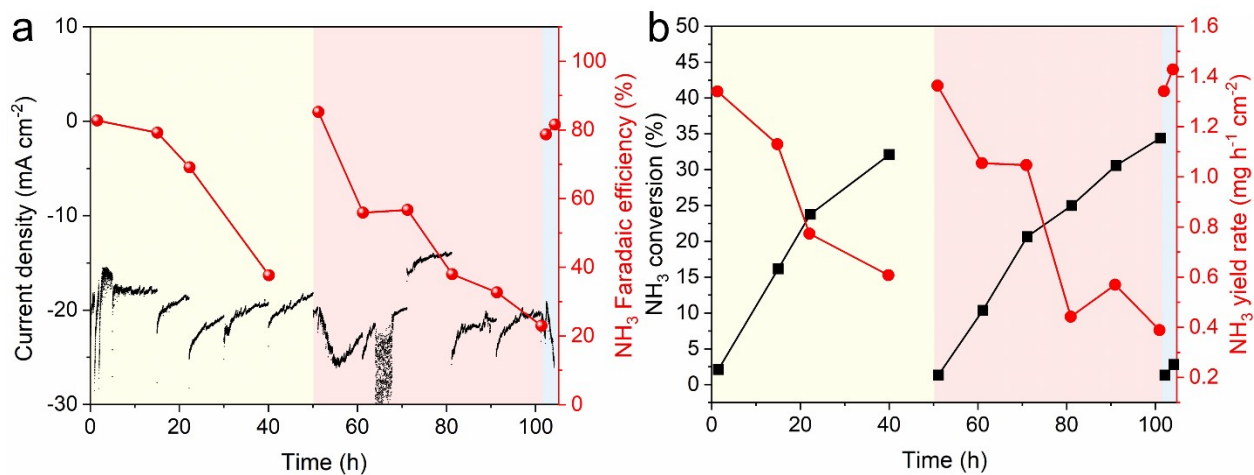


Fig. S8 Long-term e NO_3 RR stability of $\text{Cu}_{0.65}\text{Pd}_{0.35}\text{O}_x$ for 104 h. (a) Current density and NH_3 FEs. (b) NH_3 yield rate and NH_3 conversion rate as a function of electrolysis time.

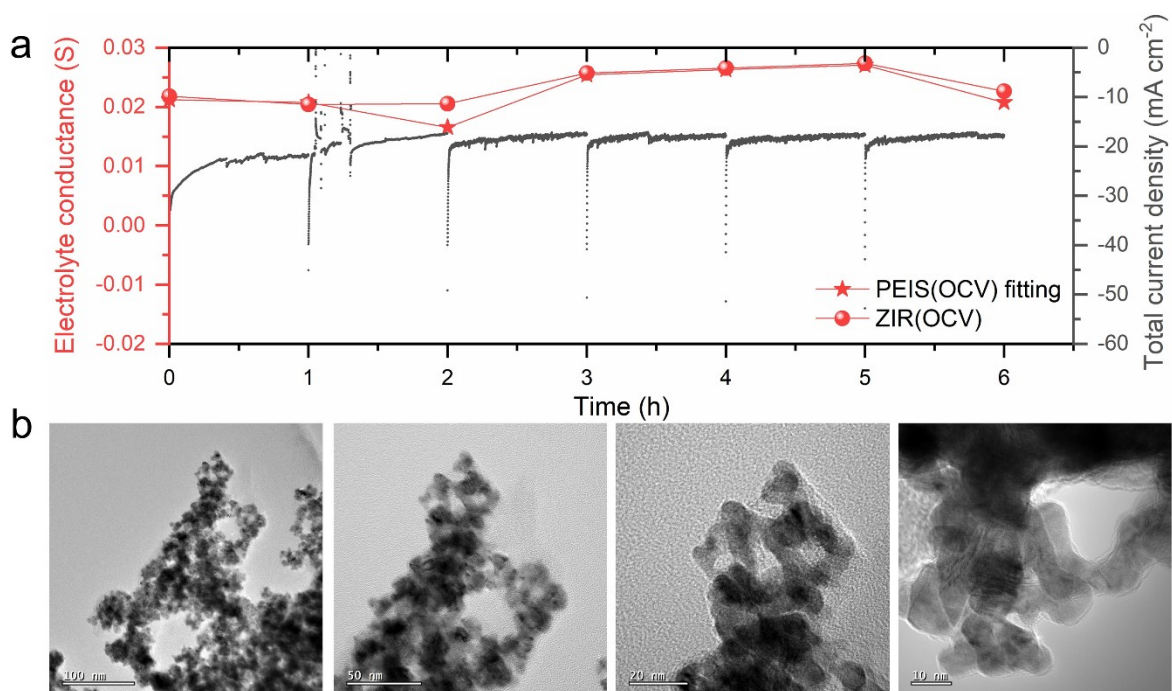


Fig. S9 (a) Traced electrolyte conductivity of 0.1 M KNO₃ during 6 h of eNO₃RR on Cu_{0.65}Pd_{0.35}O_x by using potentiostatic electrochemical impedance spectroscopy (PEIS) and impedance measurement technique (ZIR). (b) TEM images of post-reaction of Cu_{0.65}Pd_{0.35}O_x.

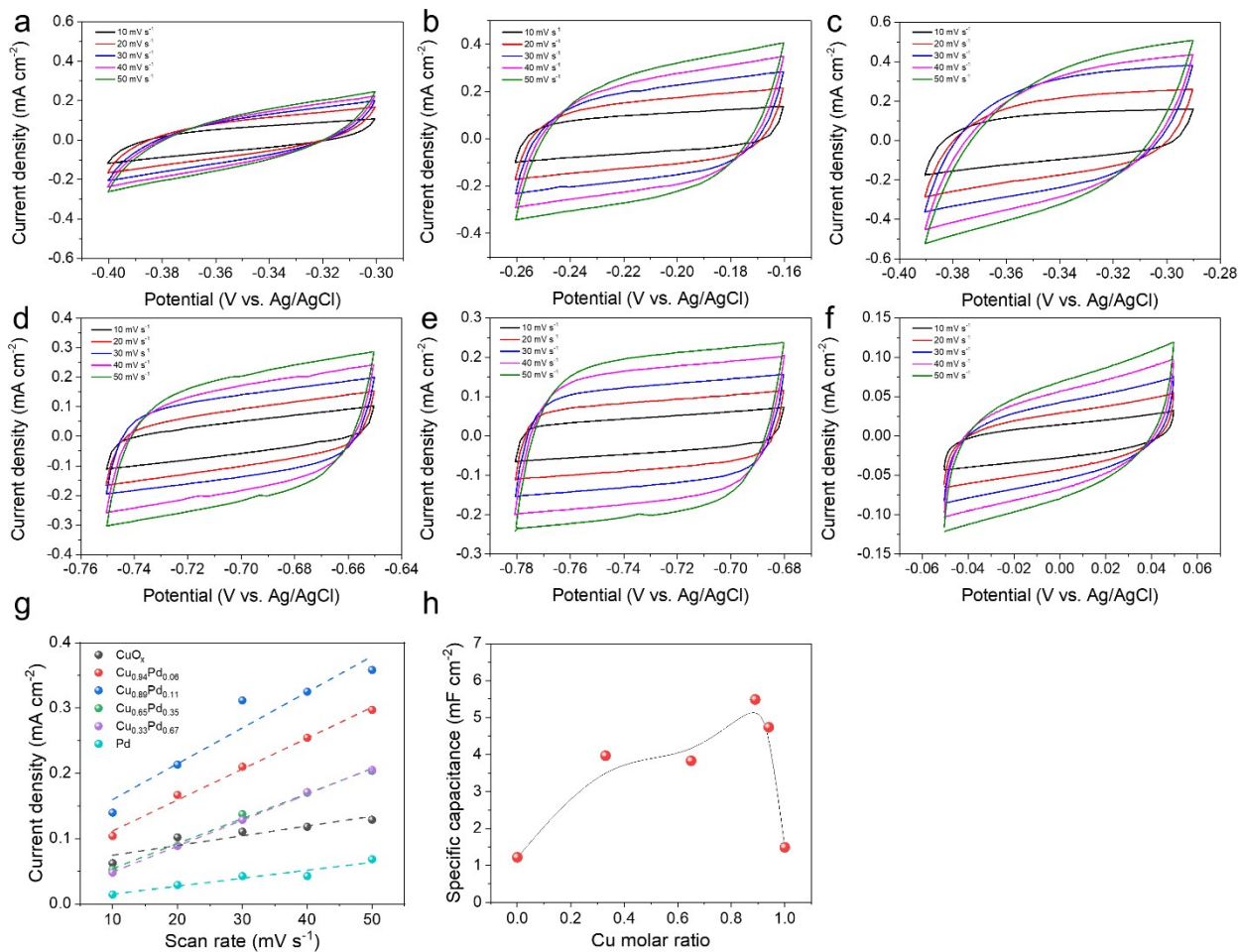


Fig. S10 Electrochemical active surface area (ECSA) obtained by cyclic voltammetry (CV) conducted with various scan rates (10, 20, 30, 40 and 50 mV s⁻¹) in 0.05 M Na₂SO₄ solution to obtain. CV profiles of (a) CuO_x, (b) Cu_{0.94}Pd_{0.06}O_x, (c) Cu_{0.89}Pd_{0.11}O_x, (d) Cu_{0.65}Pd_{0.35}O_x, (e) Cu_{0.33}Pd_{0.67}O_x, (f) Pd, respectively. (g) Current density as a function of scan rate. (h) Derived specific capacitance of CuPdO_x nanoparticles.

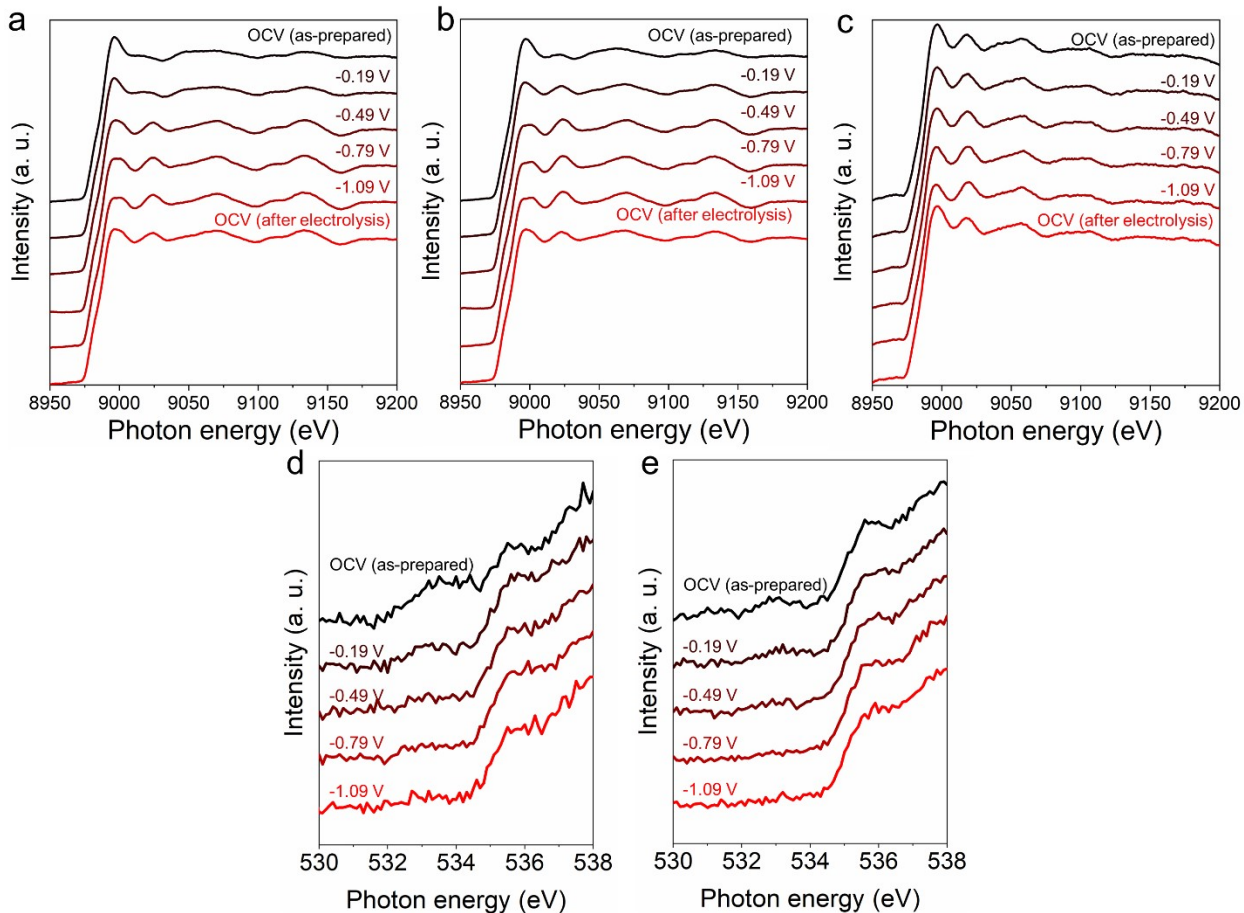


Fig. S11 *Operando* Cu K-edge XAFS profiles of (a) $\text{Cu}_{0.94}\text{Pd}_{0.06}\text{O}_x$, (b), $\text{Cu}_{0.89}\text{Pd}_{0.11}\text{O}_x$, and (c) $\text{Cu}_{0.33}\text{Pd}_{0.67}\text{O}_x$. *Operando* oxygen K-edge NEXAFS profiles of (d) CuO_x and (e) $\text{Cu}_{0.65}\text{Pd}_{0.35}\text{O}_x$ under applied potentials.

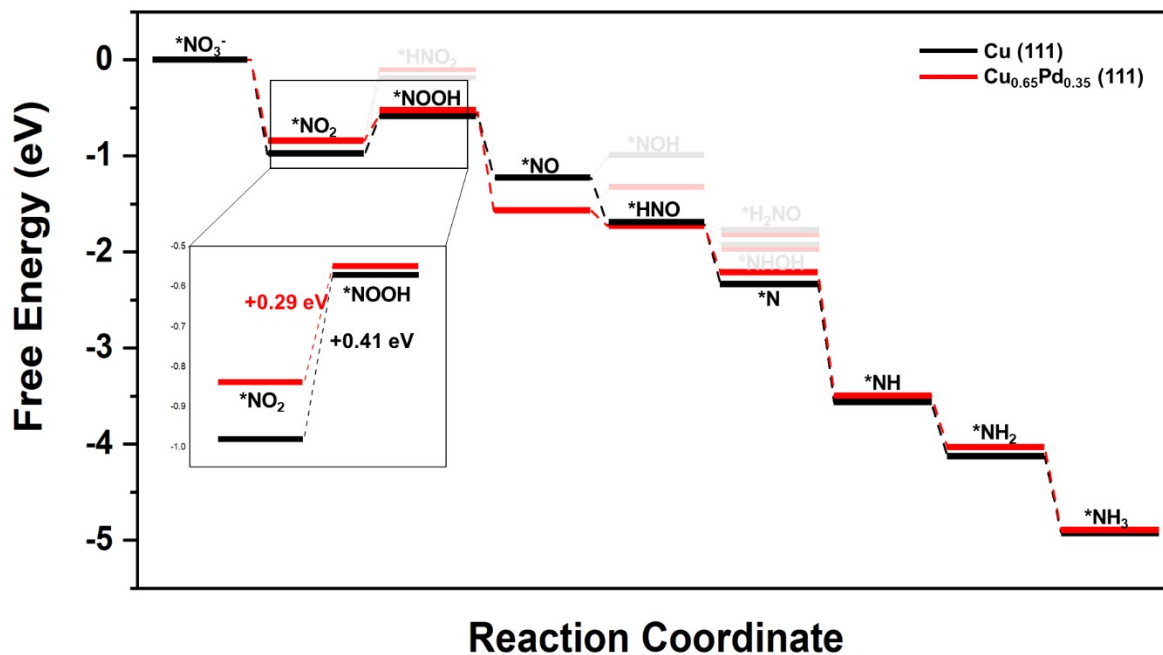


Fig. S12 Full reaction free energy diagram for the NO_3^- reduction reaction including all possible reaction intermediates.

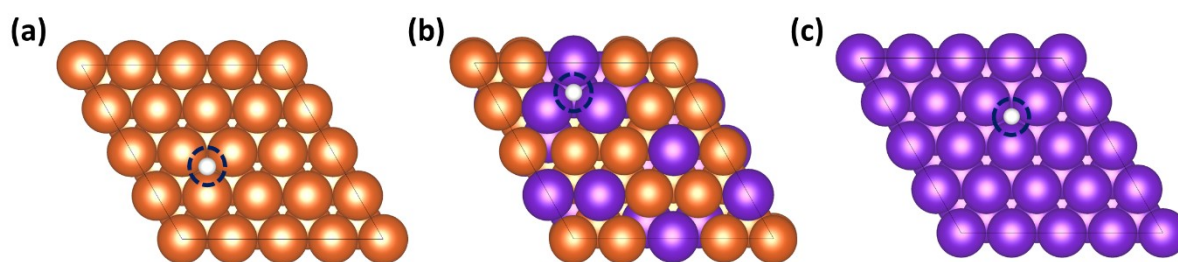


Fig. S13 The most stable hydrogen adsorption site on (a) Cu(111), (b) $\text{Cu}_{0.65}\text{Pd}_{0.35}$ (111) and (c) Pd(111) surfaces. Orange, purple and white spheres correspond to Cu, Pd and H atoms, respectively. The adsorbed H atom is highlighted with the dashed circle line.

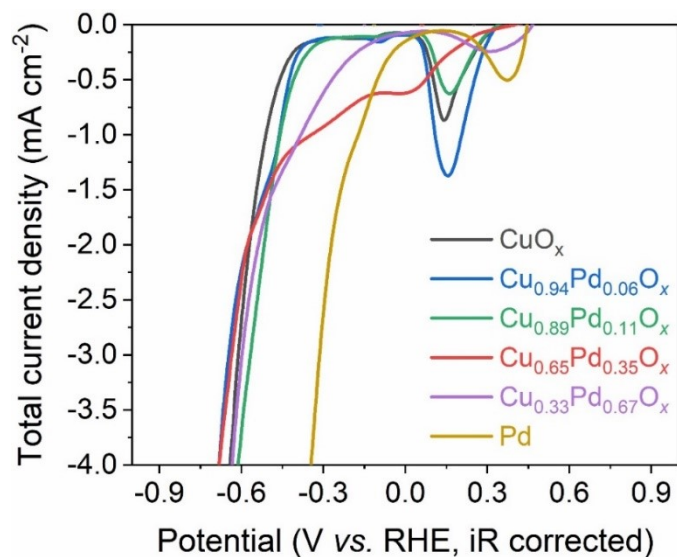


Fig. S14 LSVs of various CuPdO_x nanoparticles with 5 mV s^{-1} in $0.05 \text{ M Na}_2\text{SO}_4$ solution.

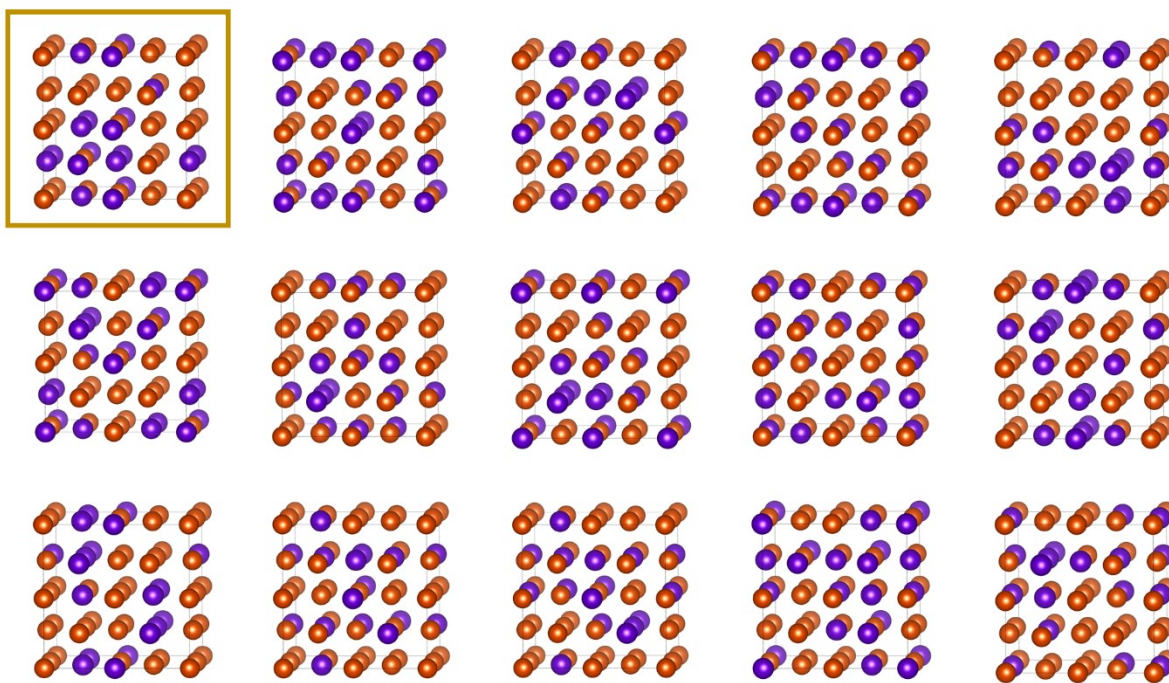


Fig. S15 The fifteen randomly generated bulk $\text{Cu}_{0.65}\text{Pd}_{0.35}$ alloy models. The model highlighted with gold solid line is the most stable one and used for the mechanism study of eNO_3RR . Orange and purple spheres correspond to Cu and Pd atoms, respectively.

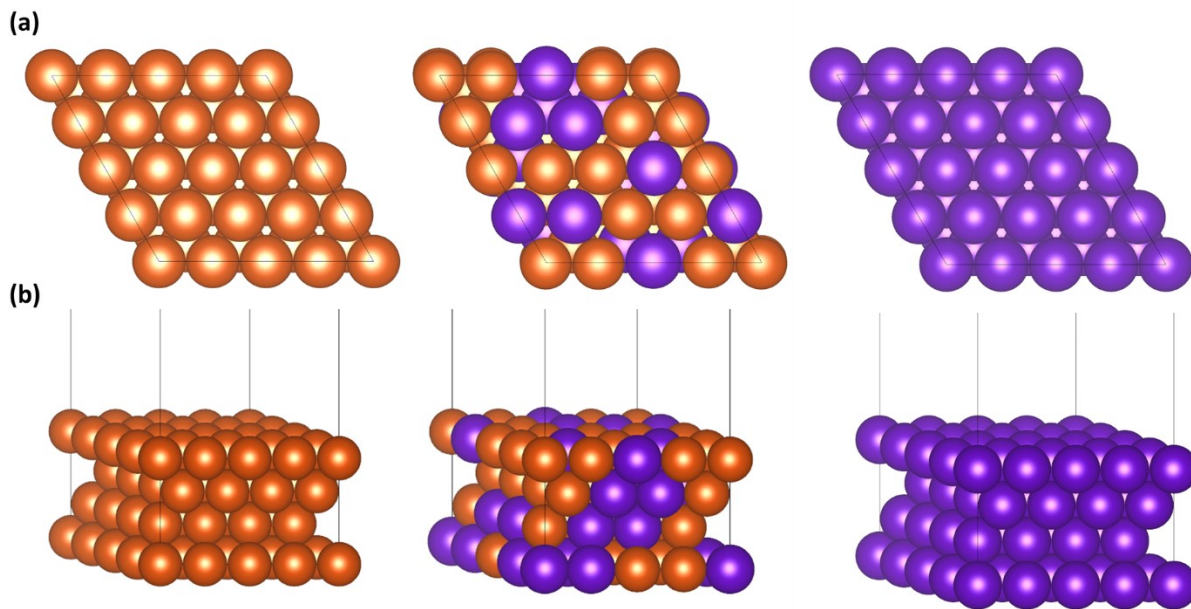


Fig. S16 (a) Top view and (b) side view of slab models for Cu (111) (left), Cu_{0.65}Pd_{0.35} (111) (middle) and Pd (111) (right) surfaces. Orange and purple spheres correspond to Cu and Pd atoms, respectively.

Supplementary Table

Table S1. Atomic ratio of Cu-Pd nanoparticles.

	EDS		ICP-OES	
	Cu (at%)	Pd (at%)	Cu (at%)	Pd (at%)
$\text{Cu}_{0.94}\text{Pd}_{0.06}$	94.1	5.9	96.1	3.9
$\text{Cu}_{0.89}\text{Pd}_{0.11}$	88.6	11.4	87.5	12.5
$\text{Cu}_{0.65}\text{Pd}_{0.35}$	65.8	34.2	63.5	36.5
$\text{Cu}_{0.33}\text{Pd}_{0.67}$	33.1	66.9	29.3	70.7

Supplementary References

1. P. E. Blochl, *Phys. Rev. B Condens. Matter*, 1994, **50**, 17953-17979.
2. J. P. Perdew, K. Burke and M. Ernzerhof, *Phys. Rev. Lett.*, 1997, **78**, 1396.
3. G. Kresse and J. Furthmuller, *Phys. Rev. B Condens. Matter*, 1996, **54**, 11169.
4. S. Grimme, J. Antony, S. Ehrlich and H. Krieg, *J. Chem. Phys.*, 2010, **132**, 154104.
5. H. J. Monkhorst and J. D. Pack, *Phys. Rev. B Condens. Matter*, 1976, **13**, 5188-5192.
6. C. Kittel, *Wiley*, 1996, **7th edn**
7. J. W. Arblaster, *Platin. Met. Rev.*, 2012, **56**, 181-189.
8. L. Vegard, *Z. Physik*, 1921, **5**, 17–26.
9. K. Mathew, V. S. C. Kolluru, S. Mula, S. N. Steinmann and R. G. Hennig, *J. Chem. Phys.*, 2019, **151**, 234101.
10. K. Mathew, R. Sundararaman, K. Letchworth-Weaver, T. A. Arias and R. G. Hennig, *J. Chem. Phys.*, 2014, **140**, 084106.